Nanoscale

PAPER

View Article Online
View Journal | View Issue

Cite this: *Nanoscale*, 2026, **18**, 5941

Spatially separated bipolar transport and surface electron accumulation in tungsten diselenide nanostructures

Hemanth Kumar Bangolla, [a] Chi-Yang Chen,[b] Cheng-Maw Cheng, [c,d,e,f] Kuei-Yi Lee,[b] Liang-Chiun Chao,†[b] Rajesh Kumar Ulaganathan,[g,h] Raman Sankar, [g] Abhishek Ghosh[i] and Ruei-San Chen *[a]

Received 4th September 2025,
Accepted 5th January 2026

DOI: 10.1039/d5nr03739e

rsc.li/nanoscale

We investigated the physical origins of the bipolar transport in nanostructured and bulk WSe_2. A high electron concentration at the surface induced by surface electron accumulation (SEA) is confirmed by angle-resolved photoemission spectroscopy (ARPES) measurements. The n-type surface coexisting with the intrinsically p-doped inner bulk of WSe_2 results in an interesting "spatially separated" bipolar transport in this layered semiconductor. The selenium vacancies at the surface are inferred to be the major cause of SEA, and their formation and passivation are highly dependent on the interaction of ambient molecules. The maximum surface electron concentration, *i.e.*, 10^{20} cm^{-3}, is approximately four orders of magnitude higher than the hole concentration of the inner bulk of WSe_2.

1. Introduction

Over the past decade, two-dimensional (2D) transition metal dichalcogenides (TMDCs) with van der Waals-layered structures have captivated profound interest from researchers in various fields[1–6] due to their intriguing properties such as tunable band gap, mechanical flexibility, moderately high carrier mobility, chemical and thermal stability, and absence of dangling bonds at their surfaces.[7,8] In TMDCs, the weak van der Waals bonded interlayers and strongly covalent bonded intralayer vary the electrical and optical properties with the number of layers.[9] To date, extensive studies have been conducted on n-type TMDCs, especially on molybdenum disulfide (MoS_2).[10] However, device applications such as solar cells, tunnel field-effect transistors (TFETs), and complementary metal–oxide–semiconductor (CMOS) circuits require a p-type TMDC material.[11] Tungsten diselenide (WSe_2) is a promising p-type material with an indirect bandgap of 1.2 eV and a direct band gap of 1.65 eV in its bulk and monolayer forms, respectively.[12–14] Zhou *et al.* observed the highest hole mobility of 100 and 350 cm^2 V^{-1} s^{-1} for the monolayer and few-layer FETs, respectively.[14] Gao *et al.* reported an ultrafast grown WSe_2 monolayer with a high hole mobility of around 143 cm^2 V^{-1} s^{-1}.[15]

The practical applications of WSe_2 devices have been complicated by the challenge of accurately adjusting the polarity of WSe_2. Ambipolar transport has been reported for WSe_2-based FET devices in literature.[16,17] Mainly, doping, contact engineering, thickness control, and plasma treatment result in unipolar or bipolar transport in WSe_2.[18–23] The admirable bipolar transport property of WSe_2 makes it an ideal candidate for complementary digital logic applications.[24–26] Researchers have extensively studied transport properties in n-type TMDCs, while only a few reports are available on the p-type variants. The precise control of the polarity in WSe_2 devices is challenging, which hinders practical applications. An extensive study is required to understand the conductivity type and the origin of n-doping and p-doping in WSe_2. Our previous studies indicate the presence of SEA in TMDCs (such as MoS_2 and $MoSe_2$) with nearly intrinsic and lightly n-doped bulk interiors.[27,28] Hence, understanding the nature of surface electron accumulation (SEA) and surface electronic transport is of great importance in the design and fabrication of high-performance WSe_2 devices.

In this work, we discover an interesting bipolar transport in WSe_2, wherein the electron and hole flows are spatially separ-

[a]*Graduate Institute of Applied Science and Technology, National Taiwan University of Science and Technology, Taipei 10607, Taiwan. E-mail: rsc@mail.ntust.edu.tw*
[b]*Graduate Institute of Electro-Optical Engineering, National Taiwan University of Science and Technology, Taipei 10607, Taiwan*
[c]*National Synchrotron Radiation Research Center, Hsinchu 30076, Taiwan*
[d]*Department of Physics, National Sun Yat-sen University, Kaohsiung 80424, Taiwan*
[e]*Department of Electrophysics, National Yang Ming Chiao Tung University, Hsinchu 300, Taiwan*
[f]*Taiwan Consortium of Emergent Crystalline Materials, National Science and Technology Council, Taipei 10601, Taiwan*
[g]*Institute of Physics, Academia Sinica, Taipei 115201, Taiwan*
[h]*Centre for Nanotechnology, Indian Institute of Technology Roorkee, 247667, India*
[i]*Institute of Atomic and Molecular Sciences, Academia Sinica, Taipei 10617, Taiwan*
†This author could not be contacted to confirm the final author list prior to acceptance.

ated in nature. SEA was also observed in WSe_2 for the first time. The spatially separated bipolar transport also results in thickness-dependent conductivity and carrier activation energy. A heavily n-doped surface with naturally occurring high electron density has been confirmed, and, on the contrary, its inner bulk is lightly p-doped. The effect of foreign molecules on the WSe_2 surface was also investigated and discussed.

2. Results and discussion

2.1 Structural and electrical analyses

Fig. 1(a) depicts the XRD pattern of a CVT-grown WSe_2 single crystal and the photograph of an as-grown bulk WSe_2 single crystal with a size of 4 mm (the inset). The crystalline structure of WSe_2 consists of five diffraction peaks positioned at 2θ values of 13.77°, 27.58°, 41.84°, 56.80°, and 72.89°, corresponding to the (002), (004), (006), (008), and (0010) planes, respectively. The obtained 2θ values are well matched with the standard JCPDS card no. 38-1388, and it reveals the 2H-phase of the WSe_2 single crystal.[29,30] The Raman spectrum of the WSe_2 single crystal is shown in Fig. 1(b), and the spectrum was deconvoluted using multi-peak Lorentz fitting. The spectrum contains two peaks, which are located at 247 and 256 cm^{-1}, with full width at half maximum (FWHM) values of 16 and 6 cm^{-1} assigned to the $E_{2g}{}^1$ and A_{1g} modes of WSe_2, respectively.[31–33] Raman measurement further confirmed the single-crystalline quality of CVT-WSe_2. Hall-effect measurements were performed to access information on the conductive type, carrier concentration, and mobility of the crystals. The pristine WSe_2 crystal shows p-type conductivity with a bulk hole concentration of $(1.27 \pm 0.21) \times 10^{15}$ cm^{-3} and mobility of 70 ± 10 cm^2 V^{-1} s^{-1}.

Fig. 1(c) illustrates the AFM height profile of the WSe_2 nanoflake on the chip template, and the inset shows the AFM image of the device. The calculated thickness of the nanoflake from the height profile was 69 nm. The *I–V* curves of the WSe_2 nanoflake devices with varying thicknesses are shown in Fig. 1(d). The linear nature of the *I–V* curves indicates the ohmic contacts between the WSe_2 nanoflakes and the Pt electrodes fabricated by FIB.[34] The top-view SEM image of the WSe_2 nanoflake device can be seen in the inset of Fig. 1(d).

2.2 Thickness-dependent conductivity and activation energy

Fig. 2(a) depicts the conductance (G) values with different thicknesses of WSe_2 nanoflakes. The conductance values are obtained from the slope of the *I–V* curves. Variations in the

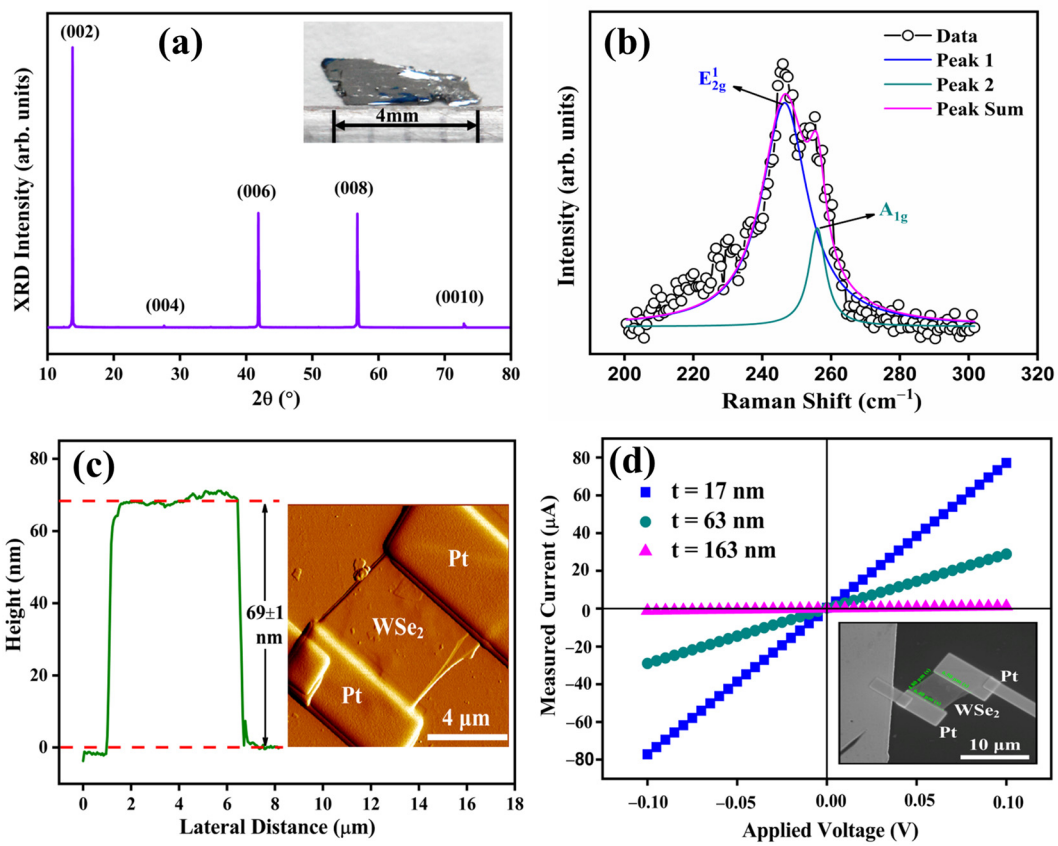

Fig. 1 (a) X-ray diffraction pattern; inset depicts the photograph of a single crystal. (b) Raman analysis for the structural characterization of the WSe_2 crystal. (c) AFM height profile of the WSe_2 nanoflake; inset shows the AFM image of the device. (d) *I–V* measurements of the WSe_2 nanoflake devices with different thicknesses; inset shows the typical top-view SEM image of the fabricated device.

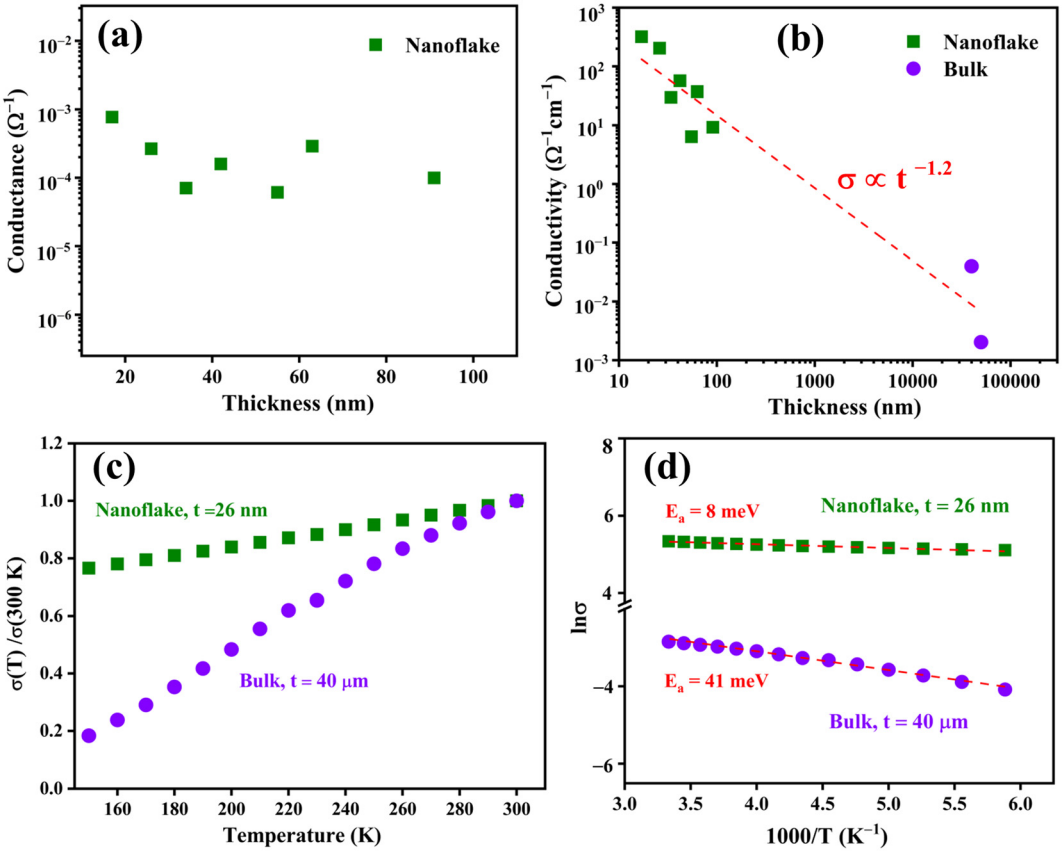

Fig. 2 (a) Plot of conductance *versus* thickness of the WSe_2 nanoflakes. (b) Plot of conductivity *versus* thickness of the WSe_2 nanoflakes and bulk crystals. (c) Temperature-dependent conductivity of the WSe_2 nanoflakes and bulk crystals. (d) Arrhenius plot ($\ln\sigma$ *vs.* 1000/T) to calculate the activation energy. The red-dashed lines denote the linear fitting of the respective data points.

thickness between 17 and 91 nm have minimal effect on the conductance values. Generally, G is linearly dependent on the thickness (t), and it is given by:[35]

$$G = \frac{I}{V} = \sigma\frac{A}{l} = \sigma\frac{wt}{l}, \quad (1)$$

where σ is the conductivity; A, w, and l are the area, width, and length of the current flow in the conductor, respectively. This near thickness-independent nature of G reveals the phenomenal change in the conductivity with changes in the thickness. To verify the dependence of conductivity on the thickness, σ was derived from eqn (1). Fig. 2(b) shows the conductivity *vs.* thickness log graph of the WSe_2 nanoflakes and bulk crystals. With the variation in thickness, the conductivity varies from 320 ± 77 to 6 ± 2 Ω^{-1} cm^{-1}. The relative contributions of the surface conductance (G_s) and bulk conductance (G_b) to the total conductance (G) are 99.94–99.98% and 0.06–0.02%, respectively. The conductivities of bulk samples with thicknesses of 40 and 50 μm are (40 ± 0.02) × 10^{-2} and (2 ± 0.01) × 10^{-3} Ω^{-1} cm^{-1}, respectively. The significant dependence of conductivity on the nanoflake thickness gives the inverse power law of $\sigma \propto t^{-\beta}$, with a β value of 1.2.

Temperature (T)-dependent conductivity measurements have been carried out for the WSe_2 nanoflake (t = 26 nm) and bulk crystal (t = 40 μm) to gain insight into the transport properties. Fig. 2(c) shows the conductivity *vs.* temperature in the range of 150–300 K. To highlight the difference between the nanoflake and bulk crystal, the curves were normalized by their σ values at 300 K. The conductivities of both the nanoflake and bulk crystal decrease with the temperature, confirming their semiconductor nature. The thermal activation energy (E_a) of the nanoflake and bulk crystal could be obtained from the following relation:[35]

$$\sigma(T) = \sigma_0 \exp(-E_a/kT), \quad (2)$$

where σ_0 is the conductivity at infinite temperature, k is Boltzmann's constant, and T is the temperature. As illustrated in Fig. 2(d), the slope of the Arrhenius plot ($\ln\sigma$ *vs.* 1000/T) can be used to calculate E_a. The calculated E_a values are 8 and 41 meV for the nanoflake and the bulk crystal, respectively. The activation energy of the bulk crystal (41 meV) is consistent with other reports for the WSe_2 crystals, for which the activation energy is in the range of 33–120 meV.[36–38] The lower E_a value of the nanoflakes compared to that of the bulk suggests that the majority of charge carriers in the nanoflakes originate from the lower donor or acceptor levels, which are different from those in the bulk. Theoretically, the nanoflakes should

have the same defect types and donor levels because they were obtained from the exfoliated bulk crystals. The lower activation energy in the nanoflakes implies that the majority carriers in the nanoflake could come from the surface rather than the inner bulk crystal.

2.3 Surface electronic structure analysis by ARPES

ARPES was utilized to study the electronic structure of the WSe_2 crystal surface under different conditions. Fig. 3(a), (b), and (c) depict the valence band ($E - E_F$ *vs.* $k_{||}$) of the *in situ*-cleaved, 4 h in air, and 3 days in air WSe_2 surfaces, respectively. Here, *in situ*-cleaved surface denotes the fresh surface created at the UHV of $<1.8 \times 10^{-10}$ Torr. When the fresh surface was exposed to an air atmosphere, an identifiable divergence in the valence band maximum (VBM) relative to the Fermi level (E_F) was seen in the band mapping images. Fig. 3(d) depicts the normal emission spectra of WSe_2 at Γ point under different surface conditions. It is evident from the enlarged normal emission spectra in Fig. 3(e) that the *in situ*-cleaved surface exhibits an abrupt valence band edge with a binding energy of −0.32 eV. The sharp valence band edge denotes the high crystalline quality of the fresh WSe_2 surface. Next, the valence band edge of the surface exposed to air for 4 h was substantially red-shifted to −1.38 eV. Upon further increasing

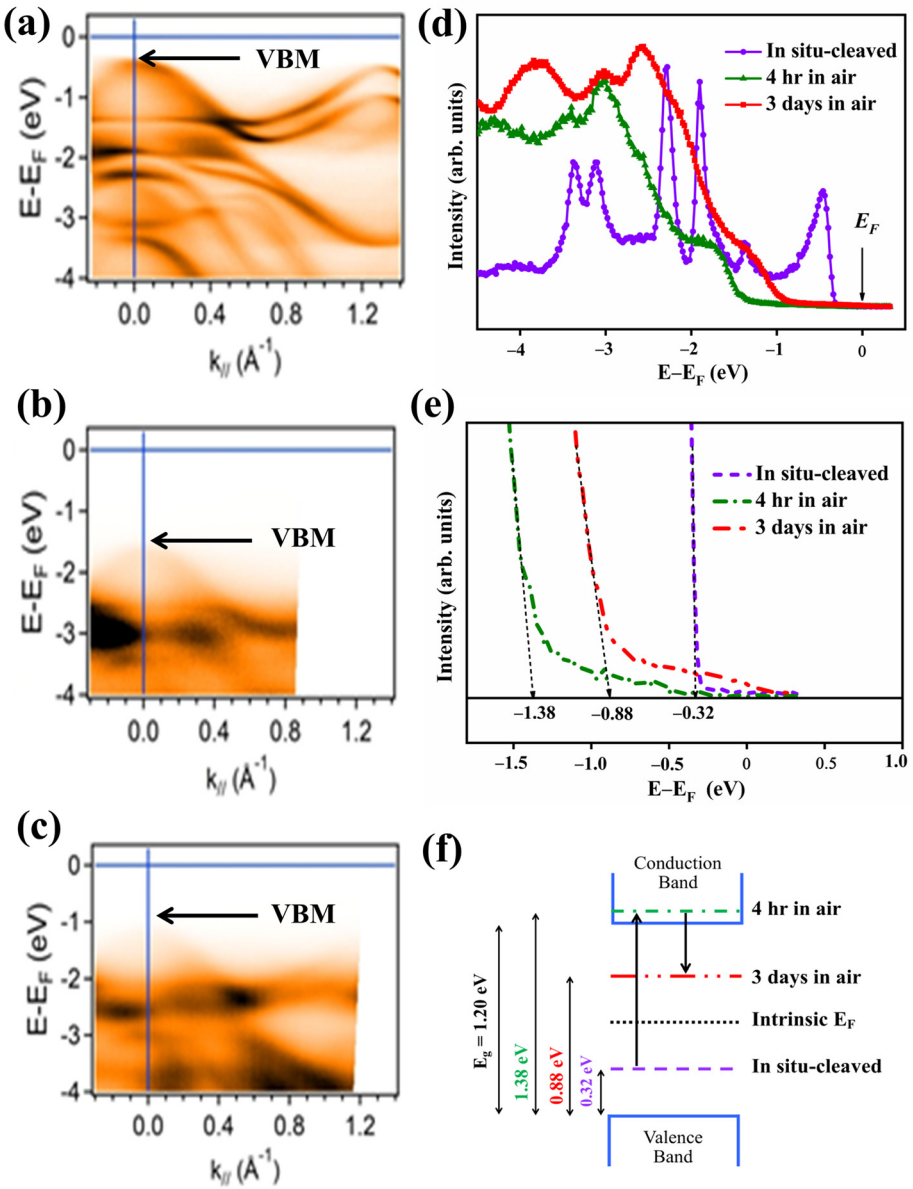

Fig. 3 ARPES characterization of the fresh and aging surfaces of WSe_2. Valence band measurement ($E - E_F$ *vs.* $k_{||}$) of the WSe_2 crystal surfaces: (a) *in situ*-cleaved, (b) 4 h in air, and (c) 3 days in air. (d) and (e) Normal emission spectra at the Γ point for the *in situ*-cleaved, 4 h in air, and 3 days in air WSe_2 surfaces with different binding energy scales. (f) Band energy diagram indicating the position of the valence band and Fermi level of different WSe_2 surfaces. The arrow marks indicate the direction of the Fermi level shift.

the air exposure time to 3 days, the valence band edge was blue-shifted to −0.88 eV. The shift in the VBM relative to the Fermi level was denoted using an energy band diagram, as shown in Fig. 3(f).

The observation indicates that the fresh surface is p-type and the air-exposed surfaces convert to n-type. The hole concentration (p) in the p-type fresh surface was calculated using the equation:[39]

$$p = N_v \exp\left[\frac{-(E_F - E_v)}{kT}\right], \quad (3)$$

where N_v is the effective density of states function in the valence band, and it is given by $N_v = 2(2m_p^* kT/h^2)^{\frac{3}{2}}$. Here, m_p^* is the effective mass of the hole, $T \sim 300$ K, and h is the Planck's constant. The energy difference $(E_F - E_v)$ is 0.32 eV, and the WSe_2 bulk bandgap is 1.20 eV.[14] The m_p^* value of $0.53m_0$ was obtained from the VBM of the *in situ*-cleaved surface measured by ARPES (see Fig. 3(a)). The parabolic fitting of the VBM is shown in Fig. S1 in SI. This value is well in agreement with the theoretical value of $0.54m_0$ for the WSe_2, where m_0 is the electron rest mass (see Table S1, SI). The calculated hole concentration for the *in situ*-cleaved surface is 4.2×10^{13} cm^{-3}. The fresh surface with a p-type nature is consistent with the result of the Hall measurement. However, the hole concentration defined by ARPES is two orders of magnitude less than the bulk value ($p \sim 10^{15}$ cm^{-3}) defined by Hall measurement. The difference may have resulted from the compensation effect, of which some n-type surface defects were created by mechanical exfoliation and coexist with the original p-type defects in the bulk.

For the surface exposed to air for 4 h, the Fermi level lies above the conduction band minimum (CBM) ($E_F - E_C = 0.18$), denoting the n-type degenerate semiconductor nature, and the electron concentration (n) of n-type degenerate semiconductors is given as follows:[28,40]

$$E_F - E_c = kT\left[\ln\left(\frac{n}{N_c}\right) + 2^{-3/2}\left(\frac{n}{N_c}\right)\right], \quad (4)$$

where N_c is the effective density of states function in the conduction band, and it is given by $N_c = 2(2m_n^* kT/h^2)^{\frac{3}{2}}$. Here, m_n^* is the effective mass of an electron, with a value of $0.60m_0$ (see Table S1, SI). A pretty high electron concentration at 1.4×10^{20} cm^{-3} is obtained, which is around six orders higher than the hole concentration of the *in situ*-cleaved surface. The electron concentration of the surface exposed to air for 3 days was calculated from the following equation.[39]

$$n = N_c \exp\left[\frac{-(E_c - E_F)}{kT}\right]. \quad (5)$$

According to the bandgap of bulk WSe_2 (1.20 eV),[14] the energy difference $(E_c - E_F)$ is 0.32 eV, m_n^* is $0.39m_0$ (see Table S1, SI). The calculated n is 2.6×10^{13} cm^{-3}. Note that the aging for 3 days did not further increase the electron concentration but instead resulted in a substantial decrease.

To clarify the effect of foreign molecules on the WSe_2 surface, ARPES was also carried out for the *in situ*-cleaved surfaces under different conditions in UHV. Fig. 4(a), (b), and (c) show the valence bands ($E - E_F$ *vs.* $k_\parallel$) of the *in situ*-cleaved, 11 days in UHV and 11 days in UHV & 15 min in air WSe_2 surfaces, respectively. Fig. 4(d) depicts the normal emission spectra of WSe_2 at Γ point under different surface conditions in the UHV environment. When the *in situ*-cleaved surface was exposed to a UHV for 11 days, the VBM shifted from −0.32 to −0.40 eV (Fig. 4(e)). This is evidence of deselenization at room temperature, which creates donor-like surface states in WSe_2 because foreign molecules are unlikely to interact with the surface in a UHV environment. Next, the surface that was kept for 11 days in UHV was subsequently shortly exposed to air for 15 min, causing a drastic shift in the valence band to −0.70 eV (Fig. 4(e)). The rapid shift in the valence band manifests that the interaction of air molecules with the WSe_2 surface could increase the deselenization rate and/or create additional surface defects, which produce more donor-like surface states.

Se vacancies in the WSe_2 surface caused by the escape of Se atoms are probably the most noticeable type of surface defects that result in the SEA phenomenon. The n-type doping due to the generation of Se vacancies in WSe_2 has been reported previously.[41,42] The SEA observed at the WSe_2 surface aging for 4 h is due to the physically adsorbed ambient molecules, such as oxygen (O_2) and water (H_2O), that speed up the deselenization and produce high-density donor-like surface states. However, the electron concentration was reduced for the surface aging for 3 days. The theoretical calculation suggests that O_2 and H_2O act as acceptor impurities in WSe_2.[43] This means that the O_2 and H_2O molecules on the surface of the WSe_2 aged for 3 days are chemically adsorbed, which results in a passivation process.

2.4 Theoretical first-principles calculations

To understand the band structure of WSe_2 under air exposure, we studied the band structure for three configurations, including pure WSe_2 (pristine); Se-vacant WSe_2 (4 h in air), which was obtained by removing one Se atom from the supercell; and *O*-substituted WSe_2 (3 days in air), in which an oxygen atom is placed at the Se vacancy site (Fig. 5). In pure WSe_2, the electronic bands around the K valley are well dispersed, resulting in relatively light and symmetric electron and hole effective masses. Introducing a Se vacancy disrupts the local W–Se coordination environment and leaves behind weakly bound electrons on the neighboring W atoms. This defect induces localized states near the conduction band edge and reduces the dispersion of both conduction and valence bands, manifested as noticeably heavier carrier effective masses. The Se vacancy acts as an electron-rich defect that promotes electron-dominated transport while suppressing hole mobility. In contrast, when the vacancy is filled by an oxygen atom, the stronger and more directional W–O bonding stabilizes the local structure and eliminates the vacancy-induced localized states. This passivation restores the intrinsic band dispersion, particularly by increasing the curvature of the valence band at K and yielding a significantly lighter

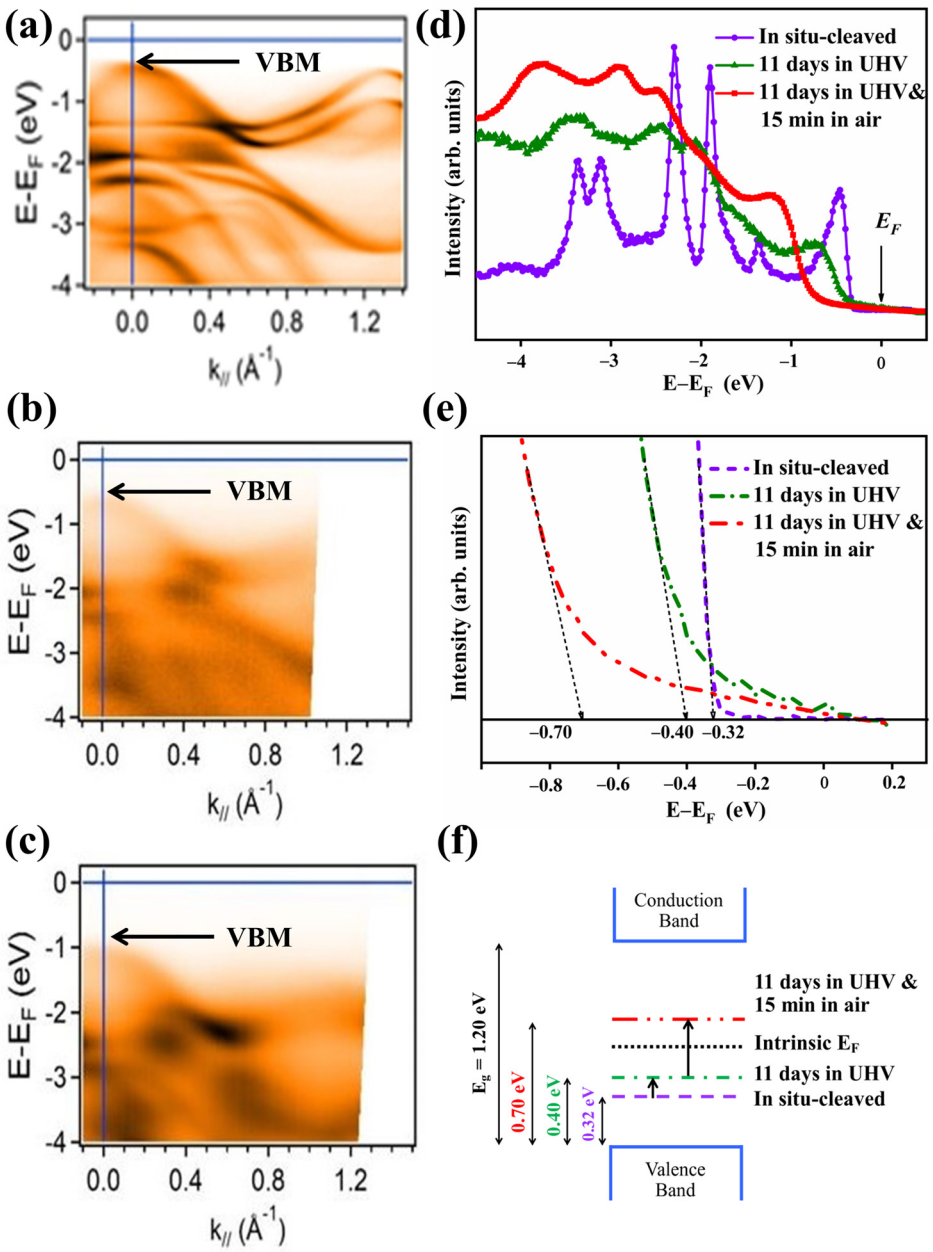

Fig. 4 ARPES characterization of WSe_2 under ultra-high vacuum (UHV) and air exposure conditions. Valence band measurement ($E - E_F$ *vs.* $k_{||}$) of the WSe_2 crystal surfaces: (a) *in situ*-cleaved, (b) 11 days in UHV, and (c) 11 days in UHV and 15 min in air. (d) and (e) Normal emission spectra at the Γ point for the *in situ*-cleaved, 11 days in UHV, and 11 days in UHV and 15 min in air WSe_2 surfaces with different binding energy scales. (f) Band energy diagram indicating the position of the valence band and Fermi level of different WSe_2 surfaces. The arrow marks indicate the direction of the Fermi level shift.

hole effective mass while recovering the original conduction band shape. As a result, the *O*-substituted system exhibits electronic characteristics that are more favorable for hole transport compared to the Se-vacant case.

2.5 SEA and bipolar transport mechanism

The nanoflakes used for the electrical measurements in this study are mostly exposed to air for less than 1 day and still exhibit strong SEA characteristics. This explains why the relatively thin nanoflakes exhibit higher conductivity in the thickness-dependent conductivity observation (Fig. 2b) among the WSe_2 nanoflakes. The surface-dominant transport is also consistent with the result of temperature-dependent electrical measurements (Fig. 2d). The majority carriers are now no longer provided by the relatively deep acceptor levels in the inner bulk but by the shallow donor states at the surface. The different origins of majority carriers further explain the different activation energy between the nanoflake and the bulk crystal.

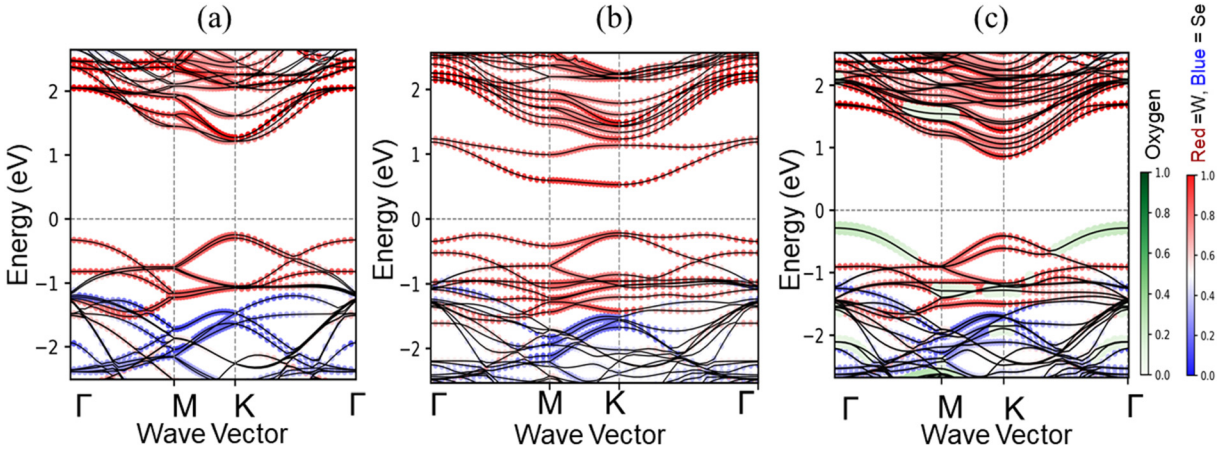

Fig. 5 Band structure of (a) pure WSe_2 (pristine), (b) WSe_2 with Se vacancy (4 h in air), and (c) WSe_2 with O_2 passivation (3 days in air).

The different majority charge carriers at the inner bulk and the surface led to spatially separated bipolar transport in WSe_2, which is schematically shown in Fig. 6(a). As we observed, electron flow dominating at the surface and hole flow dominating in the inner bulk lead to the interesting bipolar transport mechanism. Also, the schematic of the surface band bending due to SEA in WSe_2 is shown in Fig. 6(b). To maintain charge neutrality, donor-like surface states become positively charged after donating electrons to the conduction band, which causes electron accumulation at the surface and downward band bending. The Fermi level position overlapping the CBM at the surface demonstrates the high electron density at the WSe_2 surface exposed to air for 4 h according to the ARPES results.

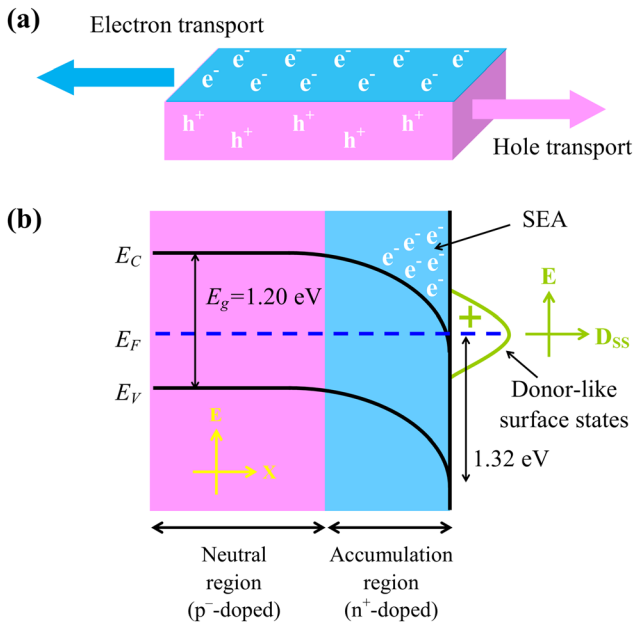

Fig. 6 Schematic of the (a) spatially separated bipolar transport mechanism and (b) surface energy band bending due to the SEA caused by the donor-like surface states in WSe_2. The Fermi level overlapping CBM at the near-surface corresponds to the *in situ*-cleaved surface according to the ARPES results.

3. Conclusions

Spatially separated bipolar transport was observed in WSe_2, where the electrons dominate at the surface and holes dominate at the inner bulk crystal. The thickness-dependent conductivity and carrier activation energy can be well explained by the unique bipolar transport. In addition, the ARPES characterization indicates the existence of SEA in WSe_2, which could be attributed to the Se vacancies. These findings provide the essential information for understanding the electrical properties of WSe_2 crystals and pave the way for their application in next-generation electronics.

4. Experimental

4.1 Crystal growth and nanoflake device fabrication

The WSe_2 single crystals were synthesized in two steps using the chemical vapor transport (CVT) method. The first step was to convert selenium powder (99.99%) and tungsten powder (99.99%) into polycrystalline WSe_2. We then subjected the polycrystalline powders to chemical vapor transport in a temperature gradient, using iodine as the transport agent. At first, the powders were mixed and placed in a quartz ampoule under a 10^{-5} Torr vacuum to mix tungsten and selenium stoichiometrically at various temperatures until near growth temperature. The generated polycrystalline powders were then employed to form single crystals by placing them in a quartz ampoule with an inner diameter of 12 mm and a length of 30 cm in the presence of a transport agent. Before being closed, the tube was evacuated once more to a pressure of less than 10^{-5} Torr. Single crystals were grown over 10 days in a two-zone furnace with a 1050 °C source and a 980 °C growth zone. During this phase, vapor transitions the polycrystalline

WSe_2 powder from a higher to a lower development temperature, where they eventually solidify to form glossy single crystals. We finally collected the WSe_2 by breaking the quartz ampoule.

The obtained WSe_2 crystals had a typical area in the mm^2 to cm^2 range, and we used them for the fabrication of the nanoflake device. First, the nanoflakes with an area in the range of micrometers and thickness in the range of a few nanometers to hundreds of nanometers were mechanically exfoliated using dicing tape from the layer crystals. Next, the individual nanoflakes were transferred onto an insulating SiO_2 (300 nm)/n^+-Si substrate chip with a pre-patterned Ti (30 nm)/Au (90 nm) circuit layout. Finally, two platinum (Pt) electrodes with a thickness of about 100–500 nm were deposited on the WSe_2 nanoflake using a dual-gun focused ion beam (FIB-FEI Quanta 3D FEG) technique. A voltage of 30 kV and a current of 100 pA were applied for the ion beam operation to decompose the Pt precursor. For the electrical characterization of the bulk crystals, silver (Ag) paste was used as the contact.

4.2 Characterization

The structural quality of the WSe_2 crystal was confirmed using X-ray diffraction (XRD-Bruker D2 Phaser) and Raman spectroscopy (Renishaw inVia Raman microscope system), with a source wavelength of 532 nm. Atomic force microscopy (AFM-Bruker Dimension Icon) was used to record the height profile of the WSe_2 nanoflakes. Scanning electron microscopy (SEM-Hitachi S3000H) was used to record the images of the device. The electrical measurements of nanoflakes were done using two probe current–voltage (*I–V*) measurement setup. The temperature-dependent conductivity measurements of the bulk crystal and nanoflake were carried out using an ultralow current leakage cryogenic probe station (LakeShore Cryotronics TTP4). A Keithley 4200-SCS semiconductor characterization equipment was utilized to source the DC voltage and measure the current.

The angle-resolved photoemission spectroscopy (ARPES) experiment was carried out using the TLS BL21B1 U9-CGM beamline at the National Synchrotron Radiation Research Center (NSRRC) in Hsinchu, Taiwan. The photoemission spectra were recorded in an ultra-high vacuum (UHV) chamber with a hemispherical energy analyzer (Scienta R4000). The different WSe_2 samples were measured at 90 K using a photon energy of 42 eV at a base pressure of 8.6×10^{-11} Torr. The beam size was approximately 100 μm, with an angular precision of 0.2° and an energy resolution better than 18 meV. The samples were loaded into a load-lock vacuum chamber and transferred to a UHV analysis chamber for preparing *in situ* and *ex situ* samples.

4.3 Computational methods

Density functional theory (DFT) calculations were performed using the Vienna *Ab initio* Simulation Package (VASP).[44] The projector-augmented wave (PAW)[45] method was employed in conjunction with the Perdew–Burke–Ernzerhof (PBE)[46] generalized-gradient approximation. A 2 × 2 × 1 bilayer WSe_2 supercell was used for all simulations, and a 10 Å vacuum spacing was added on both sides of the slab to eliminate spurious interactions between periodic images. The plane-wave kinetic-energy cutoff was set to 520 eV, and electronic self-consistency was achieved with a threshold of 10^{-6} eV. All atomic positions were fully relaxed until the Hellmann–Feynman forces on each atom were reduced below 0.01 eV $Å^{-1}$. The Brillouin zone was sampled using Γ-centered Monkhorst–Pack meshes, with a 9 × 9 × 5 grid used for structural relaxations and a denser 27 × 27 × 9 grid employed for static electronic calculations to ensure accurate eigenvalues and dispersion near the band edges. Band structures were calculated along the high-symmetry path, Γ–M–K–Γ, using a finely interpolated *k*-path to resolve changes in curvature associated with defect formation. Three configurations were investigated: (i) pristine bilayer WSe_2, (ii) Se-vacant WSe_2 formed by removing a single Se atom from the supercell, and (iii) *O*-substituted WSe_2 in which one O atom occupies the Se vacancy site. All defective structures were fully relaxed prior to electronic analyses. Carrier effective masses were extracted using the effmass package, which fits the band dispersion within ±50 meV of the conduction band minimum (CBM) and valence band maximum (VBM) to obtain reliable electron and hole effective masses.

Author contributions

Hemanth Kumar Bangolla: methodology; formal analysis; writing/original draft preparation. Chi-Yang Chen: methodology; visualization. Cheng-Maw Cheng: methodology; investigation. Kuei-Yi Lee: investigation. Liang-Chiun Chao: investigation. Rajesh Kumar Ulaganathan: investigation. Raman Sankar: investigation. Abhishek Ghosh: investigation. Ruei-San Chen: conceptualization; supervision; resources; funding acquisition; validation; writing/review and editing. All authors discussed the results and approved the final version of the manuscript.

Conflicts of interest

There are no conflicts of interest to declare.

Data availability

The data supporting this article have been included as part of the supplementary information (SI). Supplementary information is available. See DOI: https://doi.org/10.1039/d5nr03739e.

Acknowledgements

R. S. C. acknowledges the support of the National Science and Technology Council (NSTC) of Taiwan under the project (Grant No. MOST 111-2112-M-011-004-MY3, MOST 108-2628-M-011-

001-MY3, and NSTC 112-2811-M-011-002). R. S. acknowledges the financial support provided by the National Science and Technology Council (NSTC) of Taiwan under project number NSTC 111-2124-M-001-007, Academia Sinica for the budget of AS-iMATE-113-12, Center of Atomic Initiative for New Materials (AI-Mat), National Taiwan University, and the Featured Areas Research Center Program within the framework of the Higher Education Sprout Project by the Ministry of Education in Taiwan under Project No. 112L900801. R. K. U. would like to acknowledge IITR for the Faculty Initiation Grant (FIG-101068).

References

1 D. H. Kang, M. S. Kim, J. Shim, J. Jeon, H. Y. Park, W. S. Jung, H. Y. Yu, C. H. Pang, S. Lee and J. H. Park, *Adv. Funct. Mater.*, 2015, **25**, 4219–4227.
2 W. Chen, Y. Liu, Y. Li, J. Sun, Y. Qiu, C. Liu, G. Zhou and Y. Cui, *Nano Lett.*, 2016, **16**, 7588–7596.
3 J. Song, S. Kwon, M. D. Hossain, S. Chen, Z. Li and W. A. Goddard, *ACS Appl. Mater. Interfaces*, 2021, **13**, 55611–55620.
4 Q. H. Wang, K. Kalantar-Zadeh, A. Kis, J. N. Coleman and M. S. Strano, *Nat. Nanotechnol.*, 2012, **7**, 699–712.
5 A. Sanne, R. Ghosh, A. Rai, M. N. Yogeesh, S. H. Shin, A. Sharma, K. Jarvis, L. Mathew, R. Rao, D. Akinwande and S. Banerjee, *Nano Lett.*, 2015, **15**, 5039–5045.
6 Y. Kim, S. Lee, J. G. Song, K. Y. Ko, W. J. Woo, S. W. Lee, M. Park, H. Lee, Z. Lee, H. Choi, W. H. Kim, J. Park and H. Kim, *Adv. Funct. Mater.*, 2020, **30**, 2003360.
7 K. Andrews, U. Rijal, A. Bowman, H. Chuang, M. R. Koehler, J. Yan, D. G. Mandrus, P. Chen and Z. Zhou, *ACS Appl. Nano Mater.*, 2021, **4**, 5598–5610.
8 J. H. Park, A. Rai, J. Hwang, C. Zhang, I. Kwak, S. F. Wolf, S. Vishwanath, X. Liu, M. Dobrowolska, J. Furdyna, H. G. Xing, K. Cho, S. K. Banerjee and A. C. Kummel, *ACS Nano*, 2019, **13**, 7545–7555.
9 D. S. Lee, J. Y. Kim, D. Y. Shin, Y. Lee, J. Kim, S. J. Lee and J. Joo, *Adv. Electron. Mater.*, 2019, **5**, 1800802.
10 U. Krishnan, M. Kaur, K. Singh, M. Kumar and A. Kumar, *Superlattices Microstruct.*, 2019, **128**, 274–297.
11 P. M. Campbell, A. Tarasov, C. A. Joiner, M. Y. Tsai, G. Pavlidis, S. Graham, W. J. Ready and E. M. Vogel, *Nanoscale*, 2016, **8**, 2268–2276.
12 X. Wang, Y. Li, L. Zhuo, J. Zheng, X. Peng, Z. Jiao, X. Xiong, J. Han and W. Xiao, *CrystEngComm*, 2018, **20**, 6267–6272.
13 D. H. Jung, S. Kim and T. W. Kim, *Thin Solid Films*, 2021, **719**, 138508.
14 H. Zhou, C. Wang, J. C. Shaw, R. Cheng, Y. Chen, X. Huang, Y. Liu, N. O. Weiss, Z. Lin, Y. Huang and X. Duan, *Nano Lett.*, 2015, **15**, 709–713.
15 Y. Gao, Y. L. Hong, L. C. Yin, Z. Wu, Z. Yang, M. L. Chen, Z. Liu, T. Ma, D. M. Sun, Z. Ni, X. L. Ma, H. M. Cheng and W. Ren, *Adv. Mater.*, 2017, **29**, 1–8.
16 H. Fang, S. Chuang, T. C. Chang, K. Takei, T. Takahashi and A. Javey, *Nano Lett.*, 2012, **12**, 3788–3792.
17 M. I. Beddiar, X. Zhang, B. Liu and Z. Zhang, *Small Struct.*, 2022, **3**, 2200125.
18 S. Kim, C. Kim, Y. Hyun, S. Lee, M. Choi and B. Ju, *Chem. Phys. Lett.*, 2021, **770**, 138453.
19 C. Zhou, Y. Zhao, S. Raju, Y. Wang, Z. Lin, M. Chan and Y. Chai, *Adv. Funct. Mater.*, 2016, **26**, 4223–4230.
20 Y. Zhao, K. Xu, F. Pan, C. Zhou, F. Zhou and Y. Chai, *Adv. Funct. Mater.*, 2017, **27**, 1603484.
21 J. Kim, H. Park, S. Yoo, Y. Im, K. Kang and J. Kim, *Adv. Mater. Interfaces*, 2021, **8**, 2100718.
22 S. B. Mitta, F. Ali, Z. Yang, I. Moon, F. Ahmed, T. J. Yoo, B. H. Lee and W. J. Yoo, *ACS Appl. Mater. Interfaces*, 2020, **12**, 23261–23271.
23 T. Y. T. Hung, M. Z. Li, W. S. Yun, S. A. Chou, S. K. Su, E. Chen, S. L. Liew, Y. M. Yang, K. I. Lin, V. Hou, T. Y. Lee, H. Wang, A. Cheng, M. T. Lin, H. S. P. Wong and I. P. Radu, *Tech. Dig. - Int. Electron Devices Meet. IEDM*, 2022, 731–734.
24 H. Xu, X. Han, W. Liu, P. Liu, H. Fang, X. Li, Z. Li, J. Guo, B. Xiang, W. Hu, I. P. Parkin, J. Wu, Z. Guo and H. Liu, *Adv. Mater. Interfaces*, 2020, **7**, 1901628.
25 H. Qiu, Z. Liu, Y. Yao, M. Herder, S. Hecht and P. Samorì, *Adv. Mater.*, 2020, **32**, 1907903.
26 M. Stoeckel, M. Gobbi, T. Leydecker, Y. Wang, M. Eredia, S. Bonacchi, R. Verucchi, M. Timpel, M. V. Nardi, E. Orgiu and P. Samor, *ACS Nano*, 2019, **13**, 11613–11622.
27 M. D. Siao, W. C. Shen, R. S. Chen, Z. W. Chang, M. C. Shih, Y. P. Chiu and C. M. Cheng, *Nat. Commun.*, 2018, **9**, 1442.
28 Y. S. Chang, C. Y. Chen, C. J. Ho, C. M. Cheng, H. R. Chen, T. Y. Fu, Y. T. Huang, S. W. Ke, H. Y. Du, K. Y. Lee, L. C. Chao, L. C. Chen, K. H. Chen, Y. W. Chu and R. S. Chen, *Nano Energy*, 2021, **84**, 105922.
29 M. Habib, Z. Muhammad, R. Khan and C. Wu, *Nanotechnology*, 2018, **29**, 115701.
30 M. Bougouma, B. Nisol, T. Doneux, B. Guel, T. Segato, F. Reniers, M. Delplancke-ogletree, J. B. Legma and C. Buess-herman, *J. Cryst. Growth*, 2016, **453**, 111–118.
31 H. Zeng, G. Liu, J. Dai, Y. Yan, B. Zhu, R. He, L. Xie and S. Xu, *Sci. Rep.*, 2013, **3**, 2–6.
32 K. Kadiwala, E. Butanovs, A. Ogurcovs, M. Zubkins and B. Polyakov, *J. Cryst. Growth*, 2022, **593**, 126764.
33 H. Li, G. Lu, Y. Wang, Z. Yin, C. Cong, Q. He, L. Wang, F. Ding, T. Yu and H. Zhang, *Small*, 2013, **9**, 1974–1981.
34 Y. H. Huang, R. S. Chen, J. R. Zhang and Y. S. Huang, *Nanoscale*, 2015, **7**, 18964–18970.
35 R. S. Chen, C. C. Tang, W. C. Shen and Y. S. Huang, *Nanotechnology*, 2014, **25**, 415706.
36 M. K. Agarwal, V. V. Rao and V. M. Pathak, *J. Cryst. Growth*, 1989, **97**, 675–679.
37 N. Kumari, M. Kalyan, S. K. Ghosh, A. R. Maity and R. Mukherjee, *Mater. Res. Express*, 2021, **8**, 045902.
38 M. Bougouma, B. Nisol, T. Doneux, B. Guel, T. Segato, F. Reniers, M. P. Delplancke-Ogletree, J. B. Legma and C. Buess-Herman, *J. Cryst. Growth*, 2016, **453**, 111–118.

39 D. A. Neamen, *Semiconductor physics and devices:Basic Principles*, 2012.
40 S. M. Sze, *Physics of Semiconductor Devices*, 2006.
41 M. Wang, W. Wang, Y. Zhang, X. Liu, L. Gao, X. Jing, Z. Hu, J. Lu and Z. Ni, *Chin. Chem. Lett.*, 2021, **32**, 3118–3122.
42 M. Tosun, L. Chan, M. Amani, T. Roy, G. H. Ahn, P. Taheri, C. Carraro, J. W. Ager, R. Maboudian and A. Javey, *ACS Nano*, 2016, **10**, 6853–6860.
43 T. Wang, R. Zhao, X. Zhao, Y. An, X. Dai and C. Xia, *RSC Adv.*, 2016, **6**, 82793–82800.
44 G. Kresse and J. Furthmiiller, *Comput. Mater. Sci.*, 1996, **6**, 15–50.
45 P. E. Blochl, *Phys. Rev. B: Condens. Matter Mater. Phys.*, 1994, **50**, 953–979.
46 J. P. Perdew, K. Burke and M. Ernzerhof, *Phys. Rev. Lett.*, 1996, **77**, 3865–3868.